Article

Trimetallic Oxides/GO Composites Optimized with Carbon Ions Radiations for Supercapacitive Electrodes

Adil Alshoaibi [1,*], Chawki Awada [1], Faheem Ahmed [1], Raphael M. Obodo [2,3,4,5], Malik Maaza [6,7] and Fabian I. Ezema [2,6,7,8,*]

1 Department of Physics, College of Science, King Faisal University, P.O. Box 400, Al Ahsa 31982, Saudi Arabia; cawada@kfu.edu.sa (C.A.); fahmed@kfu.edu.sa (F.A.)
2 Department of Physics and Astronomy, University of Nigeria, Nsukka 410001, Nigeria; raphael.obodo@unn.edu.ng
3 Department of Physics, University of Agriculture and Environmental Sciences, Umuagwo, P.M.B. 1038 Owerri, Nigeria
4 National Center for Physics, Islamabad 44000, Pakistan
5 NPU-NCP Joint International Research Center on Advanced Nanomaterials and Defects Engineering, Northwestern Polytechnical University, Xi'an 710072, China
6 Nanosciences African Network (NANOAFNET) iThemba LABS-National Research Foundation, 1 Old Faure Road, Somerset West 7129, Somerset West P.O. Box 722, South Africa; likmaaz@gmail.com
7 UNESCO-UNISA Africa Chair in Nanosciences/Nanotechnology, College of Graduate Studies, University of South Africa (UNISA), Muckleneuk Ridge, Pretoria P.O. Box 392, South Africa
8 Africa Centre of Excellence for Sustainable Power and Energy Development (ACE-SPED), University of Nigeria, Nsukka 410001, Nigeria
* Correspondence: adshoaibi@kfu.edu.sa (A.A.); fabian.ezema@unn.edu.ng (F.I.E.); Tel.: +966-506933370 (A.A.); +234-8036239214 (F.I.E.)

Abstract: Hydrothermally synthesized electrodes of $Co_3O_4@MnO_2@NiO/GO$ were produced for use in supercapacitors. Graphene oxide (GO) was incorporated into the nanocomposites used for electrode synthesis due to its great surface area and electrical conductivity. The synergistic alliance among these composites and GO enhances electrode performance, life span, and stability. The structural properties obtained from the X-ray diffraction (XRD) results suggest that nanocomposites are crystalline in nature. The synergistic alliance among these composites and GO enhances electrode performance, life span, and stability. Performance assessment of these electrodes indicates that their characteristic performance was enhanced by C^{2+} radiation, with the uttermost performance witnessed for electrodes radiated with 5.0×10^{15} ions/cm^2.

Keywords: hydrothermal; electrodes; graphene oxide; supercapacitor; electrodes

1. Introduction

Due to the ever-increasing global population, the need for a sustainable environment, and global warming problems, the hunt for an alternative and more economical source of energy has been of deep interest [1,2]. Energy storage systems have consequently been the key target, as renewable energy generation and adoption rise. Specific applications involving electronic gadgets, electric cars, and the Internet are also increasing. These require an energy storage system with high energy density, high power density, long maintenance-free usage and stability, swift electrical response, and a wide range of operating temperatures. Thus, strategic research in supercapacitors has been hugely witnessed over the past years [3,4].

Supercapacitors possess excellent properties but lack remarkable energy density. However, it cuts the gap between conventional capacitors and batteries, which have low energy density and low power density, respectively [5]. There have been various studies aimed at improving the capacitance and energy density of supercapacitors, with a major focus

on electrode materials [6–9]. Two observable phenomena have been observed as the intrinsic mechanism of energy storage in supercapacitors; these involve electronic double layer capacitance (EDLC) and/or pseudocapacitance [10,11]. Carbon materials (activated carbon, carbon aerogels, carbon nanotubes (CNTs) or fibers (CNFs), and graphene) possess a large surface area, and store charges through the EDLC mechanism, which involves the adsorption and desorption of electrolyte ions at the electrode/electrolyte interfaces [12–14]. Transition metal oxides, sulfides, nitrides, and conducting polymers, which store charges through a fast reversible reduction–oxidation process, exhibit the pseudocapacitance mechanism [15–18]. However, carbon materials generally possess greater physical and chemical stability, a higher specific surface area, and are more conductive than pseudocapacitive materials, but they have a lower theoretical capacitance. In contrast, pseudocapacitive materials maintain higher capacitance and energy density through the faradaic process but lack good electrical conductivity [19]. Supercapacitor electrodes made with a mixture of these materials exhibit a hybrid mechanism and have been reported by several authors to show a significant improvement in the electrochemical properties [20–23].

Transition metal oxides have been deeply studied as electrode materials; they possess excellent pseudo-capacitance behavior because of their weakly oriented surface ions. Redox-active metal oxides, such as manganese oxides (MnO_2, Mn_3O_4) [24], nickel oxide (NiO) [25], nickel hydroxide ($Ni(OH)_2$) [26], cobalt oxide (Co_3O_4) [27,28], have been confirmed to offer a good specific capacitance and remarkable reversibility. Apart from these single metal oxide electrode materials, mixed metal oxides, and metal oxide composites are also excellent for electrochemical applications. These materials generally contain a high theoretical capacitance arising from their multiple oxidation states, which in turn generate a huge pseudocapacitance effect and enhance charge storage [29,30]. In contrast, the values of their practical capacitance are quite lower than the theoretical values; this is due to the reduced activity and poor electroconductivity of a single oxide. Among the techniques for modifying the electrochemical properties of metal oxides, the formation of mixed oxides, incorporation of a conductive matrix, and irradiation of the active materials have effectively optimized the energy storage capabilities of transition metal oxides. Jiani et al. [31], synthesized Co_3O_4@MnO_2 cubic nanomaterials by ZIF-67@Mn-ZIF precursor applying a facile thermal treatment. The Co_3O_4@MnO_2 electrode offered high electrochemical properties with a specific capacitance of 413 F/g at a current density of 0.5 A/g. This can be attributed to the hollow/porous configuration and high surface area of the material, which accommodate sufficient charge and discharge processes. A mixed metal oxide (Co_3O_4-MnO_2-NiO) ternary hybrid 1D nanotube electrodeposited on a gold (Au) current collector for a supercapacitor electrode was reported by Singh et al. [32]. The material recorded good electrochemical properties with a specific capacitance as high as 2525 F/g under a potential range of 0.8 V. The combined effort of these high redox metal oxides as a distinct nanostructure improved the charge retention effect of the electrode. However, a single metal oxide-based electrode, recorded by Arunpandiyan et al. [33] using MnO_2 nanorods synthesized through a hydrothermal technique, achieved a specific capacitance of 89 F/g in 1 M KOH, but improved to 634 F/g by introducing 0.1 M $K_4[Fe(CN)_6]$ redox additives into the electrolyte. Similarly, NiO film electrodeposited on an FTO glass substrate through pulse chronoamperometry yielded a high specific capacitance of up to 1000 F/g in 0.5 A/g current density [34]. While a Co_3O_4 film on a fluorine-doped tin oxide (FTO) glass substrate deposited through a potentiodynamic technique, as a supercapacitor electrode, also offered a high specific capacitance of about 397 F/g in a potential window of 1 V to −0.2 V [35]. These excellent electrochemical properties are thereby ascribed to the morphology, complex redox states, and the even thin film of the electrode material, which enhanced the electrode–electrolyte interfaces.

Compositing the metal oxides involves the use of high surface area materials, such as a carbon derivative, to act as a conductive medium for an even distribution of the metal oxide particles. This produces more active sites, with a resultant increase in the electrochemical properties. Graphene oxide is among the deeply researched components

for compositing metal oxides [36–38], with an improved capacitance and cyclic stability. Ramesh et al. [39] modified the electrochemical properties of a pure NiO/MnO_2 with that of NiO/MnO_2@nitrogen-doped graphene oxide hybrid with a specific capacitance of (266.7 to 1490) F/g at a current density of 0.5 A/g). The obtained core/shell nanocomposites displayed excellent stability with 81.7% retention capacity and proved to be a promising material for supercapacitor applications [40]. Moreso, Mary et al. [41] synthesized $rGO/NiCo_2O_4$@$ZnCo_2O_4$ (RNZC) ternary composite material for supercapacity application. The nanocomposites exhibited the best electrochemical performance because of their relatively better conductivity, high reversible charging-discharging properties, and large specific capacitance of 1197 Fg^{-1} with a maximum energy density of 62 $WhKg^{-1}$ at a current density of 1 Ag^{-1}. Similarly, the effect of N-doped activated carbon on synthesized $NiCo_2O_4$@$ZnCo_2O_4$ nanomaterial for supercapacitor devices was in [42]. The obtained hybrid composite of $NiCo_2O_4$@$ZnCo_2O_4$ with N-doped activated carbon exhibited a specific capaitance of 1029 Fg^{-1} with 78.55% capacity retention at 1 Ag^{-1}. The highest energy density and power density were 101.6 $WhKg^{-1}$ and 1.62 $W\ Kg^{-1}$, respectively.

The above synthesized composites assisted in improving the specific capacitance of the material through: (i) offering a large surface area that helped to improve the solid–electrolyte interface, which reduced the ion diffusion pathway; (ii) the composites created a channel that improved ion and electron migration, promoting easier diffusion of electrolytes, thereby utilizing the active materials in the electrode; (iii) the interconnected nanostructures yielded an improved rate stability by minimizing structural damage due to volume expansion during cycling; (iv) the obtained improved capacitance is as a result of the small diameter which resulted to a high surface area and conductivity. The crystalline nature of the nanocomposites increased the electron transfer kinetics, resulting in a high cyclability rate of the electrode.

Several researchers have proven that electron beams of sufficient energy could enhance the nanocrystalinity of activated carbon [43–45]. Electron radiation deploys a remarkable effect on the activities of the supercapacitor devices, leading to improved capacitance and conductance values by influencing the lattice structure of the electrode material irrespective of the duration of exposure to the irradiation source [46,47]. Notably, the device regained its original capacitance after removing the source of irradiation. The displayed electrochemical behavior could be attributed to the enhanced induced charges and conductance of the current collectors from the irradiation effect, which resulted in total electrode capacitance. The electron radiation affects the sp^2 states in the carbon materials and increases the electrical conductivity as the electron dose increases due to tunneling of charge carriers through nearby conductive chains [48]. The recovery of the materials' original capacitance after being removed from the radiation source is due to the inherent strength of the carbon nanostructured material to regain itself back to its original form [49,50]. The obtained results show that the electrochemical performance could be enhanced by being close to the dose of the irradiation source, and the material can regain its original capacitance value after being removed from the radiation sourcece [50]. The improved charge storage capability rate, as observed, is due to the re-modeling of the defects within the nanostructured carbon electrode material [51]. This structural distortion of carbon atoms occurred because the defect formation attained its threshold energy level and yielded a well-disordered graphite material [52]. Upon time, this defect reordered to the original formation, which resulted in a sharp drop in the discharge time while retaining its original value. To improve charge trapping and storage performance of an electrode, electron irradiation enhances carbon material charge storage through defect restructuring [53].

In this work, we studied the electrochemical properties of a conjugated $Co_3O_4/MnO_2/NiO$@GO electrode through a moderate dose of carbon ion (C^{++}) radiation. Results from the study show that induced defects within the electrodes enhanced their electrochemical performance, especially for low radiation doses.

2. Experimental Section

Chemicals used for synthesis of Co_3O_4@MnO_2@NiO/GO electrodes include cobalt chloride hexahydrate ($(CoCl_2.6H_2O)$, Sigma Aldrich, St. Louis, MO, USA, 99%) as a source of Co^+ ions, manganese (II) nitrate hexahydrate ($((Mn(NO_3)_2.6H_2O)$, Sigma Aldrich, 99%) as a source of Mn^{2+} ions for MnO_2 and nickel nitrate hexahydrate ($((Ni(NO_3)_2.6H_2O)$, Sigma Aldrich, 99%) as a source of Ni^+ ions. Sodium hydroxide solution (NaOH, Sigma Aldrich, 98%) was used as the reducing agent. FTO glass (Sigma Aldrich, 99%) is the substrate used for the fabrication of various electrodes. Carbon flakes (Sigma Aldrich, 99%) were used for the synthesis of GO. All chemicals were obtained from Shanghai, China. All reagents used in this experiment were of analytical grade and used without further purification.

### 2.1. Synthesis of Graphene Oxide (GO)

We synthesized graphene oxide (GO) using the modified hummers method. We used a carbon flake (Sigma Aldrich, 99%) to produce GO, a product of carbon, hydrogen, and oxygen. We first used hydrofluoric acid (HF) (Sigma Aldrich, 99%) to purify the carbon flake by adding 46 mL of HF acid to 2.0 g of carbon flake and stirring for 1 h to remove impurities present in the carbon flake. Double distilled water was used to wash the solution until the pH became neutral. Then, hydrogen tetraoxosulfate (IV) acid (Sigma Aldrich, 99%) was used to exfoliate the carbon flake, while using potassium permanganate (KMnO4) (Sigma Aldrich, 99%) as a catalyst and hydrogen peroxide (Sigma Aldrich, 99%) to inhibit the exfoliation. Meanwhile, after ending exfoliation with hydrogen peroxide, hydrochloric acid (Sigma Aldrich, 99%) was added, while double distilled water was later used to wash severally until the pH was neutral, before drying in an oven. The GO produced was used in the synthesis of nanostructured composites to modify its properties for various applications

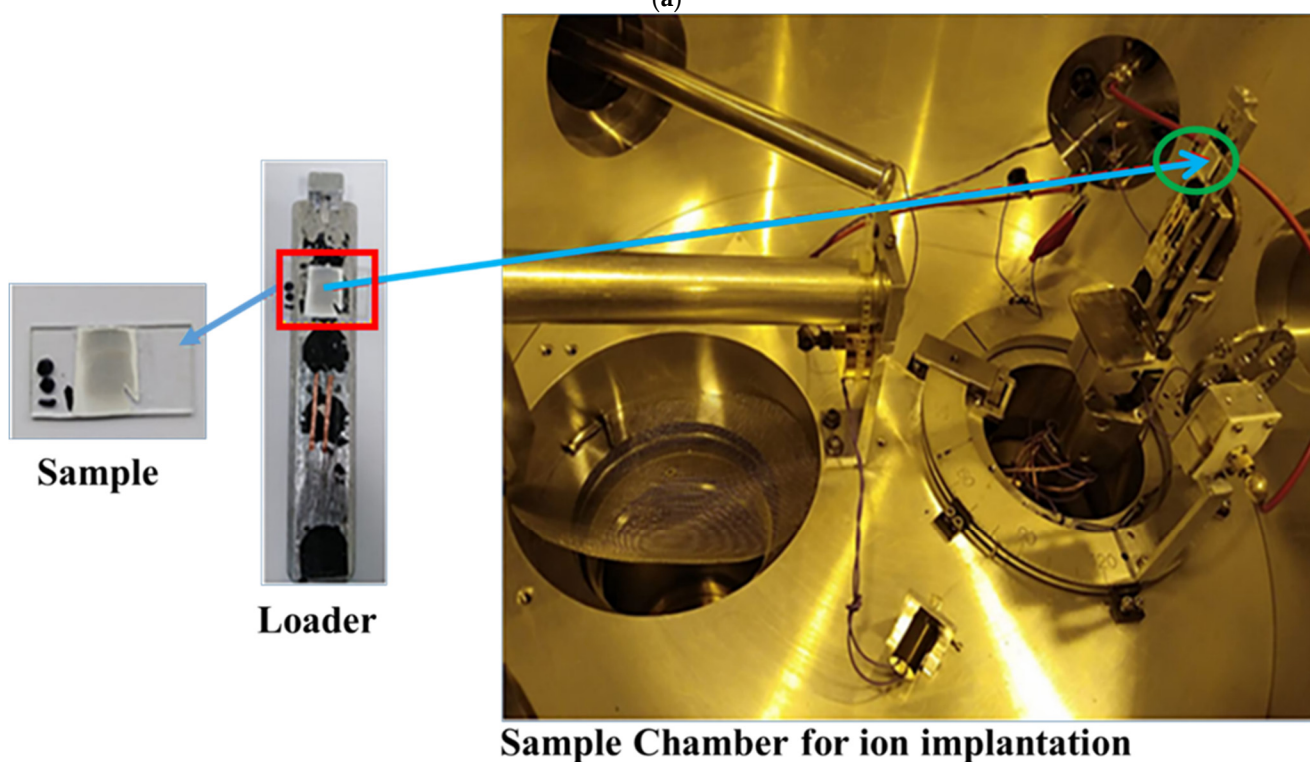### 2.2. Synthesis of Co_3O_4@MnO_2@NiO/GO Electrodes

Fifty milliliters of 0.1 M each of these three salt solutions were prepared and sonicated for 30 min separately at the ratio of 1:1:1 for Co:Mn:Ni, respectively. These three salt baths were mixed in one beaker, and 1.0 M NaOH was used to bring the mixed solution to a pH of 7. At this point, 0.05 g of GO was introduced into the mixed solution, which was sonicated for one hour to obtain homogeneity. Five pieces of fluorine tin-doped (FTO) glasses with dimensions of 1×2 cm^2 each were attached to a Teflon rod with the aid of Teflon tape, inserted inside a 300 mL autoclave, and the mixed bath was transferred inside the autoclave. The covered surface area coated with the composite is 1×1 cm^2. The autoclave was well tightened and placed inside the oven, maintaining a temperature of 180 °C for seven hours. After the end of the stipulated time, the autoclave was removed from the oven, allowed to cool down to room temperature, and dark golden electrodes were formed, as shown in Figure 1a. These electrodes were rinsed with distilled water and dried in an oven at 50 °C for one hour. Figure 1a is a sketch of the steps taken during the synthesis of Co_3O_4@MnO_2@NiO/GO electrodes.

2.3. Irradiation of Co_3O_4@MnO_2@NiO/GO Electrodes

Ion implantation is an alternative technique for introducing impurities into semiconductors. It is a more flexible approach than diffusion. It is electrically controlled by regulating voltages at slow temperature changes. Ions are channeled into a well-designed beam before accelerating to very high energies in vacuo using electric and magnetic fields. The beam in a raster is scanned on top of the target, thereby enhancing the even distribution of ions over the target surface. The ions acquire sufficient energy to diffuse into the target and collide with the lattice of the electrons due to the high accelerating voltage applied. After a while, the ion comes to rest and reunite with the electron in the lattice of the target material to form a dopant atom without any change on the path of the ion and the energy of the ion nor any damage to the crystal lattice of the atom despite the lengthy penetration duration. This process is popularly known as electronic stopping.
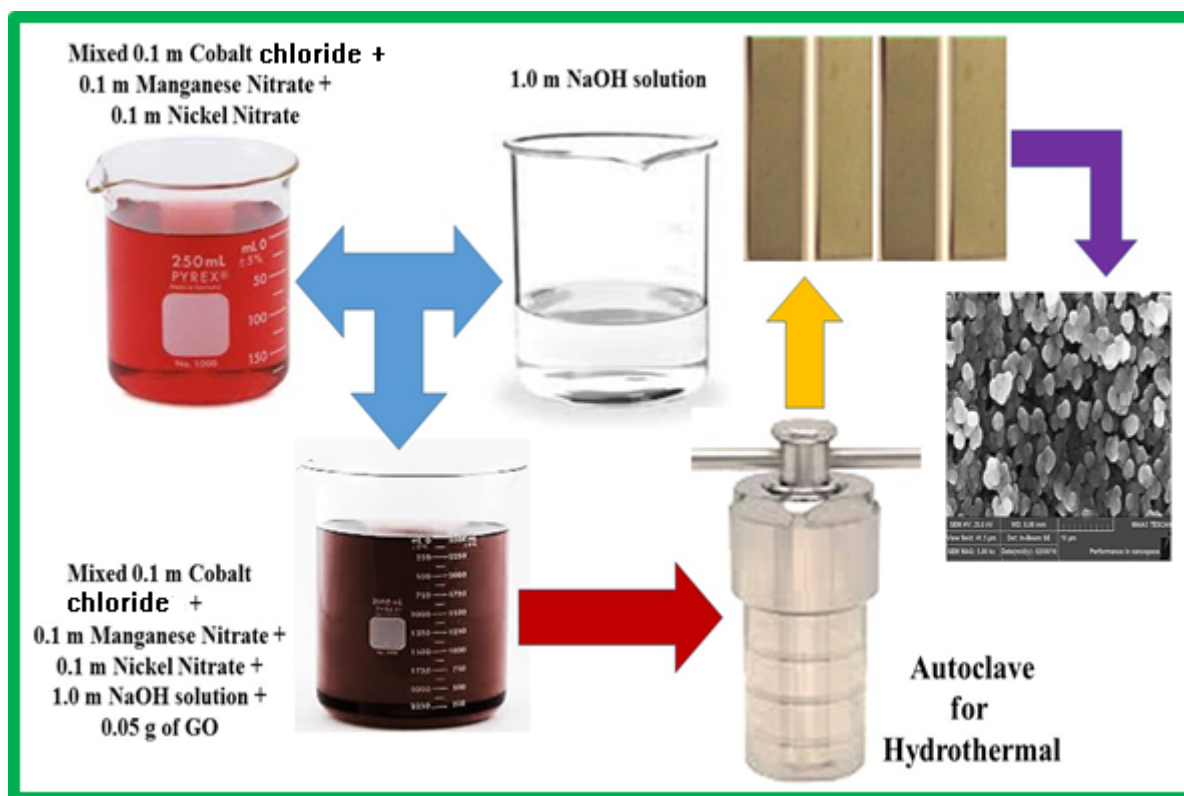
(a)

(b)

Figure 1. (**a**) $Co_3O_4@MnO_2@NiO/GO$ synthesis procedure. (**b**) Schematic procedure for ion implantation.

Electrodes of synthesized $Co_3O_4@MnO_2@NiO/GO$ composites were placed in the sample holder of a loader inside the implantation chamber [54] and radiated using 8.0 MeV

carbon ions at doses of 2.25×10^{15}, 5.0×10^{15}, 7.25×10^{15} and 1.0×10^{16} ions/cm^2 while an unirradiated electrode was kept pristine. As shown in Figure 1b, the ion current was regulated throughout the irradiation process while the chamber was maintained at a pressure of 10^{-7} Pa. The radiation of synthesized electrodes was conducted using a Pelletron Tandem accelerator installed at the Experimental Physics Department (EPD), National Center for Physics (NCP), Islamabad, Pakistan.

2.4. Electrodes Characterizations

The structural phases of Co_3O_4@MnO_2@NiO/GO electrodes were studied by X-ray diffraction using a Rigaku Miniflex-600 X-ray diffractometer with copper radiation (Kα of $\lambda = 0.154$ nm) at a scanning speed of 1° per minute within the $10-70°$ 2θ range. Fourier transform infrared (FTIR) spectroscopy was used to study functional groups and bonding features of Co_3O_4@MnO_2@NiO/GO, measured within the $500-4000$ cm^{-1} wavelength range on an Alpha (II) Bruker instrument using KBr pellets at room temperature. The surface morphology features of Co_3O_4@MnO_2@NiO/GO was measured using field emission-scanning electron microscopy (FE-SEM) (model JSM-7001F, JEOL) equipped with energy-dispersive X-ray spectroscopy (EDS). GUPIXWIN computer software was used to study the PIXE spectrum, while RUMP computer software was used to study the RBS. Electrochemical characterization was performed using Gamry 3000 electrochemical workstation equipment in a 1.0 M NaOH electrolytic solution.

3. Results and Discussions

3.1. Structural Analysis

Figure 2 shows the crystal structure of hydrothermally synthesized GO with the peak at 2θ = 11° with (001) plane and 2θ = 26.62° with (002) plane, which confirms the graphene oxide formation. While Figure 3 shows the crystal structure of Co_3O_4@MnO_2@NiO/GO composite displayed distinguishing diffraction crests of $CoMn_2O_4$ (Co_3O_4/MnO_2) composite with JCPDS card numbers of 01-077-0471 possess peaks at 31.74°, 32.80°, 34.40°, 36.08°, 39.44°, 41.49°, 47.49°, 56.60°, and 62.79° with reflection planes of (200), (103), (013), (210), (120), (212), (023), (303), and (321) respectively. Similarly, it also exhibited diffraction peaks of $NiMn_2O_4$ (MnO_2/NiO) composite with a JCPDS card number of 00-001-1110 with recorded peaks angles at 31.74°, 35.01°, 36.16°, 56.52°, and 62.79° with reflection planes of (220), (311), (222), and (440), respectively. However, it also demonstrated distinctive diffraction peaks of $NiCo_2O_4$ (Co_3O_4/NiO) composite with a JCPDS card number of 01-073-1704, recording peaks at 31.74°, 32.89°, 41.47°, 47.58°, 58.55°, and 62.79° with reflection planes of (311), (222), (331), (422), (531), and (533), respectively. Various peaks of Co_3O_4@MnO_2@NiO/GO were sharp, strong, and fine, indicating the good crystallinity nature of the composite nanostructure, prompting possible long cycle life and stability of the fabricated sample electrodes during electrochemical processes [55]. The perceived peaks and crystal planes showed the creation of tetragonal $CoMn_2O_4$ with a = b = 4.9330 Å, c = 13.7100 Å, $\alpha = \beta = 90°$, $\gamma = 120°$, Cubic $NiMn_2O_4$ with a = b = c = 8.3820 Å, $\alpha = \beta = \gamma = 90°$ and Cubic $NiCo_2O_4$ with a = b = c = 9.3872 Å, $\alpha = \beta = \gamma = 90°$ phases.

There was a graphene oxide peak at 2θ = 10.85° in the pristine sample irradiated with 2.25×10^{15} ions/cm^2 carbon ions, confirming the presence of GO. There was a small increase in the intensities of various peaks of the nanostructured electrodes after irradiating with a carbon ion dose of 2.25×10^{15} ions/cm^2, and the GO peak moved from 10.85° to 25.10°, showing movement from GO to rGO (reduced graphene oxide). However, various peak intensities also increased promptly and sharply after an increase in carbon ion radiation to 5.0×10^{15} ions/cm^2. The increase in the intensity of peaks at the 2.25×10^{15} and 5.0×10^{15} ions/cm^2 dosages indicates recrystallization and improved the crystalline nature because carbon ion radiation transported energy to the electrode's lattices and stimulated recrystallization. This was also an increase in radiation doses to 7.25×10^{15} and 1.0×10^{16} ions/cm^2. Various peak intensities decreased as radiation dose increased, while

rGO peak remained at its 2θ peak position but also decreased as radiation doses increased. These observed features indicate disintegration, dislocation, and defect creation at higher carbon ion radiation quantities [56,57]. We used the Debye Scherrer equation to estimate electrode crystallite size (D) using the most intensified peak. The acquired crystal sizes were 12.25, 8.86, 7.44, and 3.55 nm for pristine, doses of 2.25×10^{15}, 5.0×10^{15}, 7.25×10^{15} and 1.0×10^{16} ions/cm^2 respectively. We also estimated dislocation density (δ), number of crystals per unit area (N), and microstrain (ε) using XRD data employing Equations (1)–(3).

$$\delta = \frac{1}{D^2} \tag{1}$$

$$N = \frac{d}{D^2} \tag{2}$$

$$\varepsilon = \frac{\beta Cos\theta}{4} \tag{3}$$

where D is the crystallite size, d stands for film thickness, β represents FWHM and θ stands for value 2θ angle. Variation in structural parameters was estimated and is shown in Table 1. The d-spacing of 0.24 nm corresponds to the (311) lattice plane of the Co_3O_4 crystal, and the d-spacing of 0.22 nm relates to the (200) lattice plane of the MnO_2 crystal.

Table 1. Calculated structural parameters of Co_3O_4@MnO_2@NiO/GO electrodes.

S/N	Electrode/ Radiation Dose (ions/cm^2)	Dislocation Density (δ) (10^{17}m)	Number of Crystallites in a Unit Surface Area (N) (10^{-12}m)	Microstrain (ε) (10^{-2})
1	Pristine	0.56	1.79	4.20
2	2.25×10^{15}	1.25	4.74	6.27
3	5.0×10^{15}	2.07	7.29	8.18
4	7.25×10^{15}	8.90	32.04	11.26
5	1.0×10^{16}	9.10	33.66	13.77
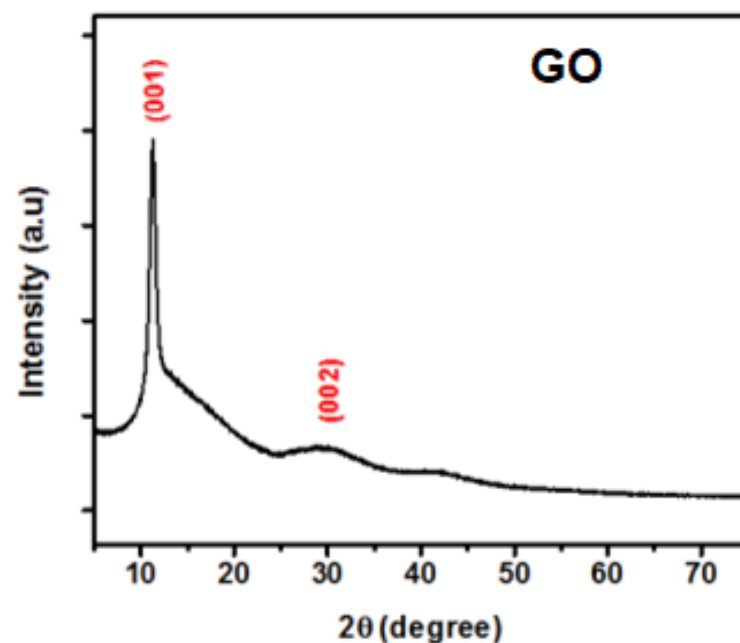
Figure 2. XRD spectra of hydrothermally synthesized GO.
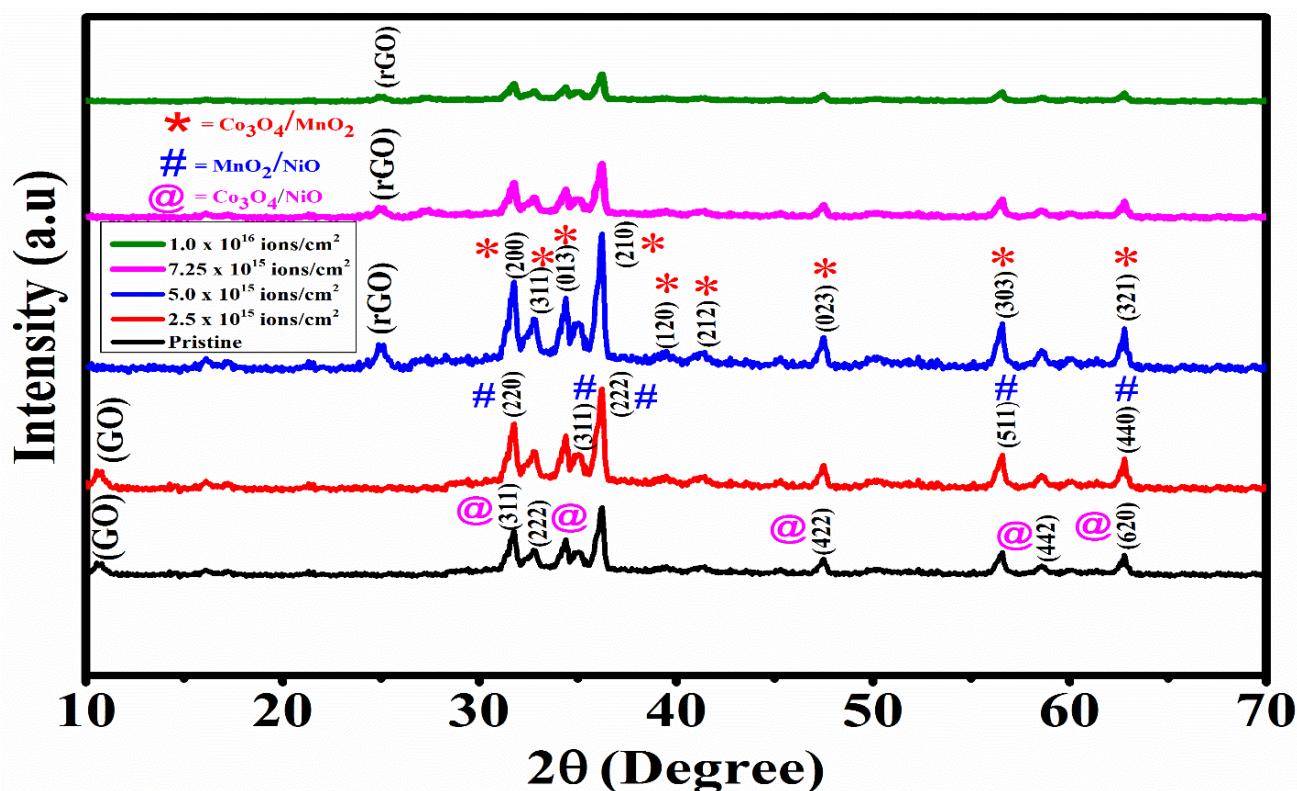
Figure 3. XRD spectra of Co_3O_4@MnO_2@NiO/GO electrodes.

3.2. Surface/Morphological Analysis

The morphology and microstructure of Co_3O_4@MnO_2@NiO/GO electrodes were studied using SEM. Figure 4a is the SEM image of the pristine electrode, which demonstrates that the pristine electrode possesses a mixture of flake and granular particles evenly distributed on the surface of the substrate. The shapes were randomly distributed on the surface of the substrates. These flake- and granular-shaped particles are small in nature, which can be credited to the condensed crystallite feature of these particles. On the other hand, larger and uniformly dispersed spherical-shaped particles were observed in Co_3O_4@MnO_2@NiO/GO electrodes irradiated with 2.25×10^{15} ions/cm^2 as shown in Figure 4b, displaying an improved feature after reception of radiation. The SEM micrograph in Figure 4c reveals the surface morphology of Co_3O_4@MnO_2@NiO/GO electrode radiated with a 5.0×10^{15} ions/cm^2 dose, this electrode showed uniformly, enhanced, well-defined, and evenly distributed spherical particles. This awesome crystalline feature indicates that this radiation dose is the ideal radiation dose for optimal crystalline nature. The SEM feature presented in Figure 4d reveals the surface morphology of Co_3O_4@MnO_2@NiO/GO electrode radiated with a 7.25×10^{15} ions/cm^2 dose, there is shrinkage of various particles after radiation. The highly conglomerated nanocomposite has a high crystallite structure with pores on the surfaces of substrates [58]. Simply treating a nanoporous carbon with gamma irradiation alters its lattice morphology with ionizing radiations that generate free radicals within the material.

The elemental distribution of the deposited MnO_2@NiO@GO nanocomposite on the glass substrate surface is shown in Figure 4f. The figure reveals different percentage distributions of elements, which are 56 and 44% corresponding to manganese (Mn), and nickel (Ni) in that order.
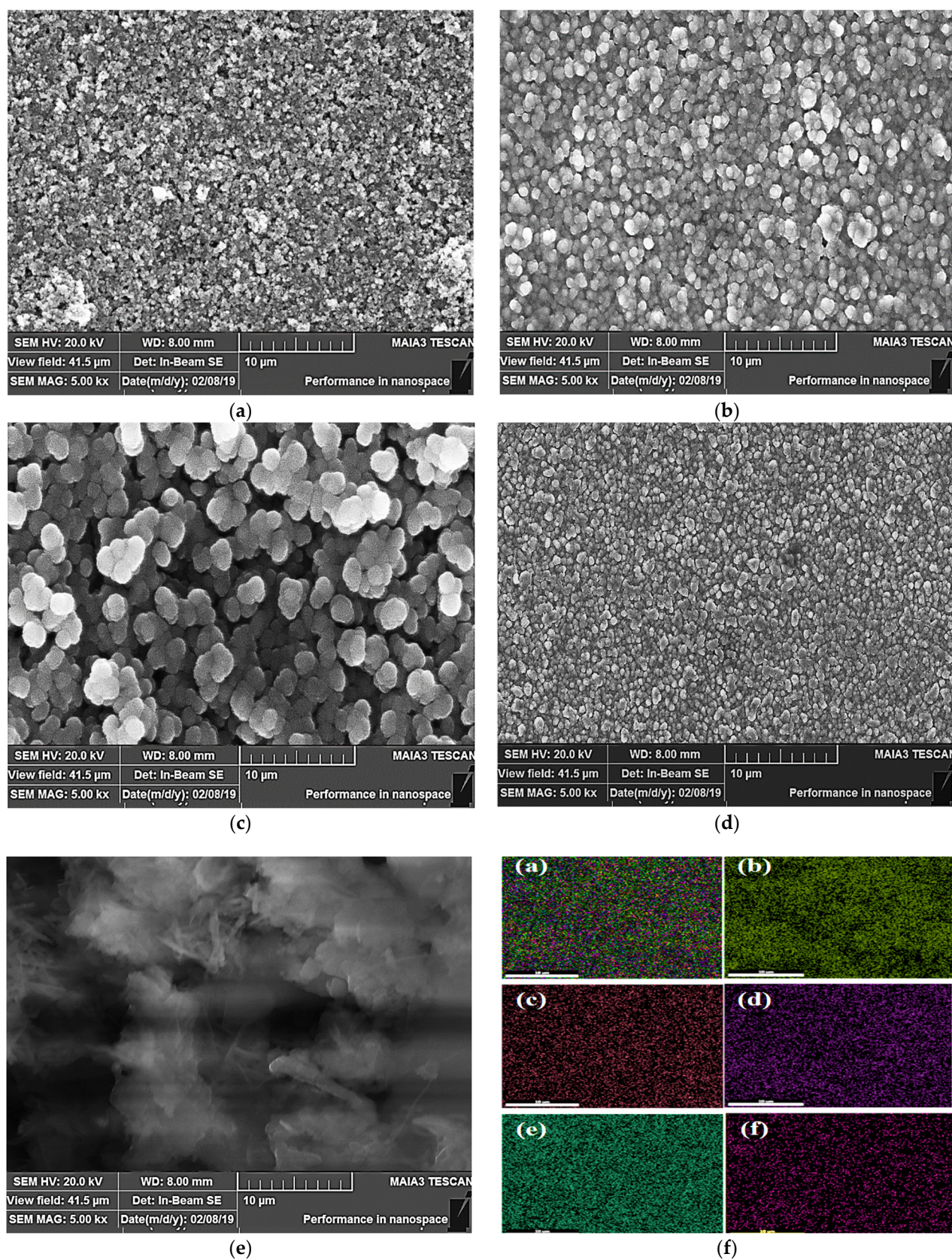
Figure 4. SEM micrographs of (**a**) pristine (**b**) radiation dose of 2.25×10^{15} (**c**) 5.0×10^{15} (**d**) 7.25×10^{15} (**e**) 1.0×10^{16} ions/cm^2 and (**f**) EDS elemental composition of (**a**) Composite (**b**) O$_2$ (**c**) Co (**d**) Mn (**e**) Ni (**f**) Cl.

Figure 5a presents the EDS outline of the $Co_3O_4@MnO_2@NiO/GO$ pristine electrode. The existence of Co, Mn, and Ni crests showed that the electrodes were effectively fabricated with their corresponding metal nanoparticles, while Cl confirms the presence of chlorine obtained from $CoCl_2 \cdot 6H_2O$. The manifestation of oxygen peaks with very prominent intensities indicates that the electrodes were efficaciously converted to their respective metal oxide forms. The FTIR spectrum of the $Co_3O_4@MnO_2@NiO/GO$ pristine electrode is presented in Figure 5b. The peak located at 3445.69 cm^{-1} indicates a stretching vibration of the O-H (hydroxide) functional group. The peak that appeared at 1789.81 cm^{-1} in the electrode signifies a symmetric stretching of the C-O-H group. Various characteristic peaks observed between 300–1000 cm^{-1} for the composite's electrode denote stretching and vibration of metal oxides (Co_3O_4, MnO_2, and NiO), while peaks observed between 500–700 cm^{-1} indicate a bending and vibration of metal oxides (Co_3O_4, MnO_2, and NiO) bonds.
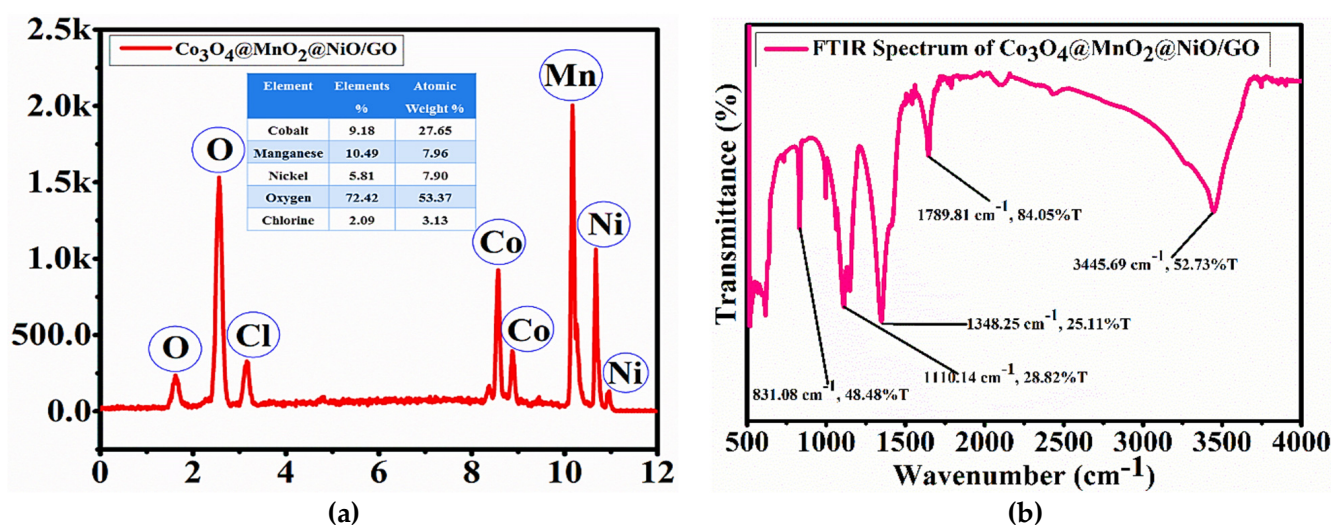

Figure 5. (**a**) EDS and (**b**) FTIR Spectra of Pristine $Co_3O_4@MnO_2@NiO/GO$ Electrode.

Figure 6a and b shows the proton-induced X-ray emission (PIXE) and Rutherford backscattering (RBS) spectra of Pristine $Co_3O_4@MnO_2@NiO/GO$ Electrode. GUPIXWIN computer software was used to study the PIXE spectrum, which reveals the peaks and percentage weight distribution of the sample elements, as can be seen in Table 1, while RUMP computer software was used to study the RBS, which reveals the energy and channel distribution of the sample elements, as observed in Table 2. Elemental distribution of Co, Mn, Ni, and minor traces elements of Cl was observed, with Mn having the highest percentage weight, energy, and channel distribution. This result confirms the supremacy of Mn, as observed in the EDS and XRD outcomes. Tables 2 and 3 present a review of PIXE and RBS elemental configurations. This displayed the absolute thickness and composition of the thin films.

Table 2. PIXE spectra parameters for Pristine $Co_3O_4@MnO_2@NiO/GO$ Electrode.

Elements	Mass	% Weights by PIXE
Co	54.94	22
Mn	65.37	48
Ni	63.50	30

Table 3. RBS spectra parameters for Pristine $Co_3O_4@MnO_2@NiO/GO$ Electrode.

Elements	Mass	K (ion)	Energy (MeV)	Channel
Co	54.94	0.7885	1.618	1618.49
Mn	65.37	0.7485	1.556	1556.06
Ni	63.50	0.7540	1.630	1629.90

(a)

(b)
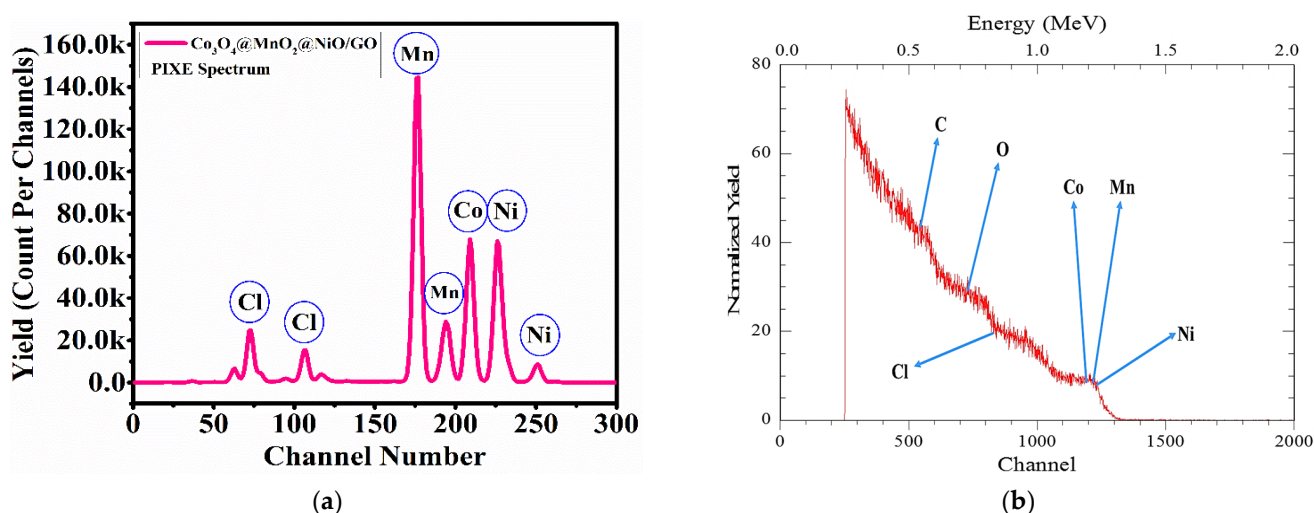
Figure 6. Spectra of (**a**) PIXE and (**b**) RBS of Pristine $Co_3O_4@MnO_2@NiO/GO$ Electrode.

3.3. Electrochemistry Analysis

We operated three electrode systems having $Co_3O_4@MnO_2@NiO/GO$ fabricated working electrodes, graphite counter electrodes, and an Ag/AgCl reference electrode. Many researchers have reported the electrochemical performances of several carbon-based nanostructured materials, such as Co_3O_4, MnO_2, and $Co_3O_4@MnO_2$ core/shell [59–61]. During the electrode–electrolyte reaction, there is an obvious display of metal oxide and various oxidation states (Co^{3+}/Co^{4+}) by the cobalt (Co_3O_4) and MnO_2 materials. From previous results, the electrochemical properties of nanostructured $Co_3O_4@MnO_2@NiO/GO$ electrodes were studied in a three-electrode configuration for CV, GCD, and EIS analysis. The commonly known three electrodes set up consisted of Pt electrode, $Co_3O_4@MnO_2@NiO/GO$ composite, and Ag/AgCl as counter, working, and reference electrodes, respectively. To narrate the growth mechanism of $Co_3O_4@MnO_2@NiO/GO$ composite on FTO, several cyclic voltammetry reports on bare FTO have shown that a rapid decrease in the current density from the maximum potential window has been observed [62,63]. This is evident that the CV of the bare FTO does not contribute to the resultant CV of the composite electrodes.

The measurement was performed in a 1.0 M NaOH aqueous electrolyte at room temperature in the potential windows 0–0.8 V vs. SCE with an electrode with an active mass of 0.45 mg. A NaOH solution of 1.0 molar concentration was employed as an operational electrolytic solution at various scan rates values of 1.0, 2.0, 3.0, 4.0, 5.0, 6.0, 7.0, 8.0, 9.0, and 10.0 mVs^{-1} and potential window of 0 to 0.7 V, as shown in Figure 7a–d, the obtained CV curves looks alike which is an evident of the irreversible nature of the $Co_3O_4@MnO_2@NiO/GO$ composite except in Figure 7d where there is an observed distinct redox activity during the cathodic and anodic sweepings for the 7.5×10^{15} radiation dose sample. This was a result of less polarization or oxygen evolution effect after irradiation, which led to the shrinkage of various particles, as confirmed by the SEM result. The CV curves obey the charge/discharge process of $Co_3O_4@MnO_2@NiO/GO$ composite through the redox reaction (faradaic reaction) at the electrode–electrolyte interface. From the electrochemical behavior of Co_3O_4, MnO_2, $Co_3O_4@MnO_2$, Co_3O_4, MnO_2, and $Co_3O_4@MnO_2@NiO$, the non-faradaic activity is due to the double layer capacitance, while

the faradaic reaction involves the ion diffusion from the electrode to the electrolyte due to the surface bound mechanism. Therefore, CV is a product of the accumulated charge during the faradaic and non-faradaic processes [64–66]. The invented electrodes have shown judicious features such as their specific capacitance, energy density, and power densities [9,44,67], as shown in Figure 7a–e and using Equations (6)–(8) [6,7].

The specific capacitance values of various electrodes fabricated were deducted from CV curves using Equation (4).

$$C_{sp} = \frac{1}{mVs} \int I(V)dV \ (F/g) \tag{4}$$

where m is the active mass in mg, V is the potential window used in volts, s is the sweep rate in mVs^{-1} and I is the current applied in ampere (A).

$Co_3O_4@MnO_2@NiO/GO$ electrodes with $1.0 \ mVs^{-1}$ rate of the scan revealed the utmost specific capacitance of 563, 641, 732, 467, and 215 Fg^{-1} for pristine, electrodes radiated with $2.5 \times 10^{15}, 5.0 \times 10^{15}, 7.5 \times 10^{15}, 1.0 \times 10^{16}$ ions/cm^2 dosages of radiation, respectively. A distinct redox peak noticed during the cathodic and anodic sweepings for the 7.5×10^{15} ions cm^{-2} radiation dose sample can be attributed to recrystallization due to an increased dose of carbon ions. This agrees with the XRD results in Figure 3. It is evident from the result that the 5.0×10^{15} ions/cm^2 radiated electrodes have the best specific capacitance. The results also indicate that at high-energy doses, specific capacitance decreased. This also confirms the high level of defects formed at high-energy dosages. The resistance and reaction kinetics of the electrodes were obtained from the EIS study. The EIS was carried out from the frequency boundary between 1.0 and 100.0 kHz, as shown in Figure 7e. A CPE diffusion model was used to study the resistances of the fabricated electrodes. The CPE model consented greatly with the Nyquist plot of the EIS. The resistances of electrolytes (Re) are 2.15, 2.55, 1.06, 3.02, and 4.80 ohms for pristine sample and $2.5 \times 10^{15}, 5.0 \times 10^{15}, 7.5 \times 10^{15}$ and 1.0×10^{16} ions/cm^2 doses respectively. However, resistances of working electrodes (Rw) are 0.09, 0.06, 0.035, 0.17, and 1.05 ohms for the pristine electrodes radiated with $2.5 \times 10^{15}, 5.0 \times 10^{15}, 7.5 \times 10^{15}$, and 1.0×10^{16} ions/cm^2 dosages of energy, respectively. Various acquired electrode resistances were low, an attribute of unification of GO in the course of fabricating these electrodes. The addition of GO improved electrode conductivities, hence reducing resistance. The Nyquist plots of $Co_3O_4@MnO_2@NiO/GO$ electrodes were void of a semi-circle, indicating that electrodes possess low charge transfer resistance [2,9,68,69].

The GCD plots of $Co_3O_4@MnO_2@NiO/GO$ electrodes shown in Figure 8a,b for current densities of 1.0 and 2.0 A/g disclose non-linear inclined voltage vs time variations [70]. Specific capacitance values were calculated using GCD plots and with the help of Equation (5).

$$C_{sp} = \frac{I \int V dt}{ms\Delta V} \ (F/g) \tag{5}$$

where m stands for active mass in mg, ΔV denotes potential window in volts, dt is the discharge time in seconds, I is the current in ampere (A), and s is a constant. The estimated specific capacitance values from the GCD plots were 503, 697, 811, 842, and 472 Fg^{-1} for the pristine and electrodes irradiated with $2.5 \times 10^{15}, 5.0 \times 10^{15}, 7.5 \times 10^{15}$, and 1.0×10^{16} ions/cm^2 dosages, respectively, using a $1.0 \ Ag^{-1}$ current density. While at $2.0 \ Ag^{-1}$ current density, the specific capacitance values for the pristine and electrodes irradiated with $2.5 \times 10^{15}, 5.0 \times 10^{15}, 7.5 \times 10^{15}$, and 1.0×10^{15} ions cm^{-2} dosages were 425, 572, 640, 658, and 399 Fg^{-1}, respectively. These results seamlessly agree with Pawar et all [71] and Li et al. [72]. The specific capacitance style attained in CV examinations was also persistent in GCD investigation. There was a voltage drop observed in the GCD plots, especially for 2.0 A/g current density. A voltage drop is caused by losses because of resistances accessible by the electrolytic solution and commonly holds an important value after numerous charge and discharge successions, symbolized by aging in-

cidences [73]. Table 4 shows the assessment of electrochemical performance of synthesized MnO_2-based electrocatalysts as investigated in comparison with this current research.
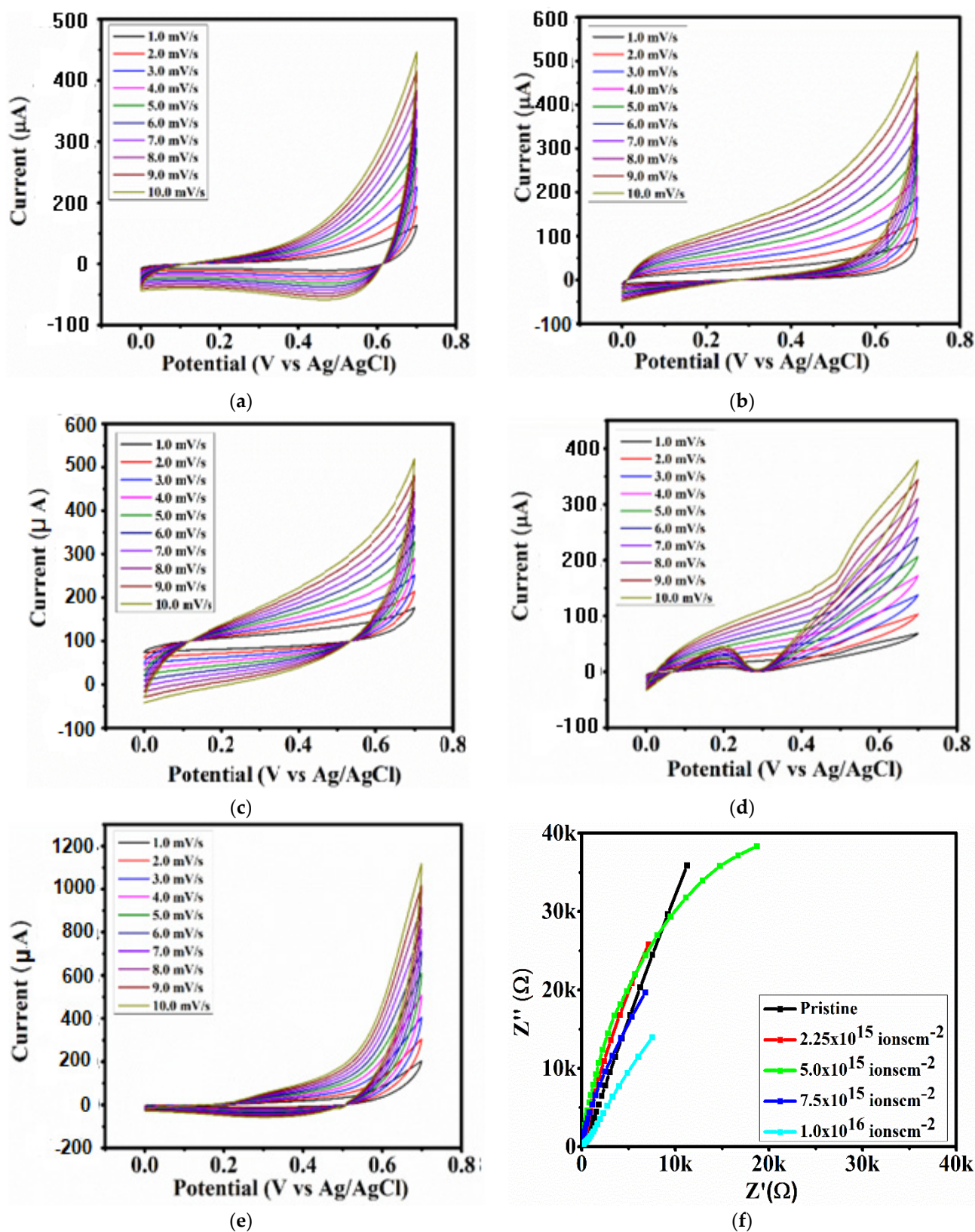

Figure 7. CV of $Co_3O_4@MnO_2@NiO/GO$ Electrodes for (**a**) pristine samples radiated with (**b**) 2.5×10^{15}, (**c**) 5.0×10^{15}, (**d**) 7.5×10^{15}, (**e**) 1.0×10^{15} ions/cm^2 energy and (**f**) EIS.
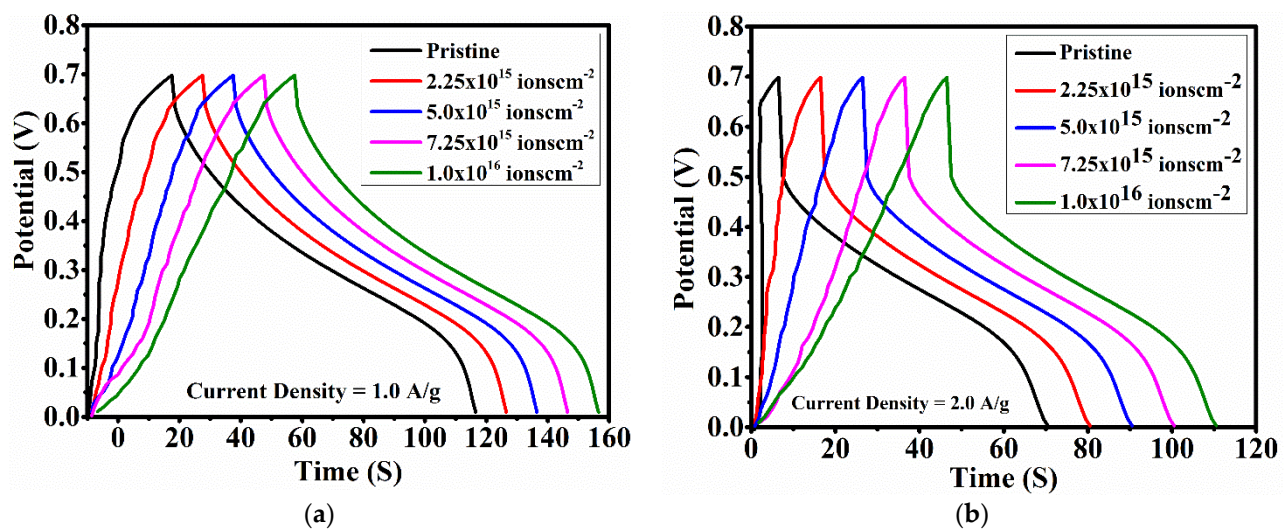
Figure 8. GCD Plots of $Co_3O_4@MnO_2@NiO/GO$ electrodes at (**a**) 1.0 A/g and (**b**) 2.0 A/g.

We also carried out more evaluation of the properties of $Co_3O_4@MnO_2@NiO/GO$ electrodes by estimating energy (E_d) and power (P_d) densities using Equations (8) and (9) [5,6,8].

$$E_d = 0.5 \times C_s \, (\Delta V)^2 \tag{6}$$

$$P_d = 3.6 \frac{t_D}{t_C} \tag{7}$$

where t_D denotes the time to discharge, ΔV is the potential window and t_D represent time to charge. The energy densities estimated were 296.70, 368.48, 451.78, 233.98, and 199.92 Whkg^{-1} for pristine electrodes and electrodes radiated with 2.5×10^{15}, 5.0×10^{15}, 7.5×10^{15}, and 1.0×10^{16} ions/cm^2 dosages, respectively. The power densities achieved were 30.40, 32.44, 40.55, 28.52, and 16.11 Wkg^{-1} for the pristine electrode and electrodes radiated with 2.5×10^{15}, 5.0×10^{15}, 7.5×10^{15}, and 1.0×10^{16} ions/cm^2 dosages of energy, respectively.

The cycle stability and efficiency of $Co_3O_4@MnO_2@NiO/GO$ electrode radiated with a dosage of 5.0×10^{15} ions/cm^2 delivering a superior feature was analyzed using a current density of 1.0 A/g for continuous 10,000 cycles, as shown in Figure 9. $Co_3O_4@MnO_2@NiO/GO$-enhanced electrodes showed good cyclic stability and possessed a capacitive retention of 93.9% after 10,000 continuous cycles. This was obtained using Equation (9) [74]. However, this electrode displayed enhanced stability after receiving energy from the carbon ions. The coulombic efficiency of ions/cm^2 radiated $Co_3O_4@MnO_2@NiO/GO$ electrode was estimated using the formula shown in Equation (8). The calculated coulombic efficiency (η), which describes the efficiency and rate of charge transfer in a system. This parameter quantifies electrochemical reactions, as well as energy storage devices [39].

$$\eta = \frac{T_d}{T_c} \times 100\% \tag{8}$$

where T_d and T_c represents time to discharge and charge, respectively.

$$\text{Capacitance Retention (\%)} = \frac{stable\ capacitive\ value\ or\ last\ cycle\ capacitive\ value}{Real\ or\ first\ capacitive\ value} \times 100 \tag{9}$$
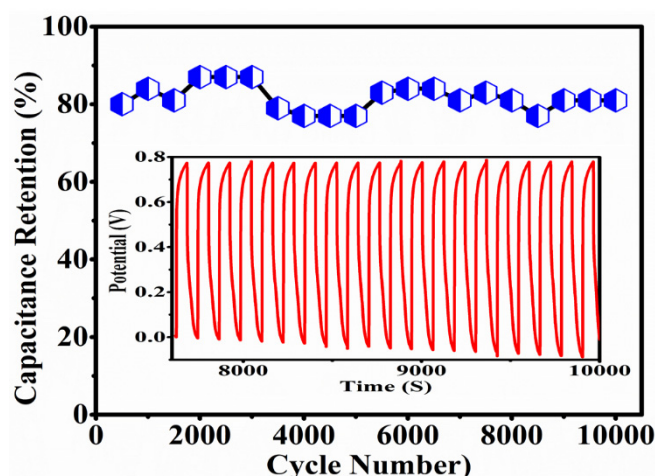
Figure 9. Plots of Specific capacitance versus scan rates of the electrodes with stability test as an inset.

Table 4. Comparison of the supercapacitor values of various nanostructured cobalt oxides (Co_3O_4), Manganese oxides (MnO_2) and Co_3O_4@MnO_2/GO electrodes reported in the literature.

S/NO	Composites	Morphology	Specific Capacitance (Fg^{-1})	Current Density (Ag^{-1})	Potential Window (V)	Ref.
1.	$Ni(OH)_2$-MnO_2	nanoflake core–shell	355	0.5	−0.1–0.9	[75]
2.	MnO_2/NiO	nanoparticle	681	1	−1–0.9	[76]
3.	Ni–Mn	hedgehog-like hollow	1016	0.5	−0.2–1.0	[77]
4.	MnOOH/NiO	nanosheets	1625	4	0–0.6	[78]
5.	Co_3O_4/NiO/MnO_2	nanospheres	549	0.5	−0.4–0.6	[32]
6.	Co_3O_4@MnO_2/NGO	nanosheet	347	0.5	−0.34–0.34	[36]
7.	Co_3O_4@Pt@MnO_2	nanoflakes	593	1	0–1.0	[79]
8.	NiO@Co_3O_4@MnO_2	nanoflakes	792.5	2	0.35–0.5	[80]
9.	Co_3O_4@MnO_2@PPy	nanoflakes	977	1	0–0.8	[81]
10.	Co-Ni/Co_3O_4-NiO	Nano heterostructure	2013	2.5	0.1–0.5	[82]
11.	Co_3O_4@MnO_2	nanowire	413	0.5	0–0.6	[31]
12.	α-MnO_2 and Co_3O_4	Microspheres	214.6	3		[83]
13.	rGO/$NiCo_2O_4$@$ZnCo_2O_4$	nanosheets	1197	1	0–0.55	[41]
14.	Co_3O_4-MnO_2-NiO	nanotubes	2525	15	−0.2–0.6	[32]
15.	$MnCO_3$ QDs/NiH–Mn–CO_3	shell–nanoneedle	2641.3	3	−0.2–1.0	[84]
16.	NiO-Co_3O_4	mesoporous	324	2	−0.5–0.5	[85]
17.	Co_3O_4@MnO_2@NiO/GO	nanosphere	215–732	1	0–0.8	This work

4. Conclusions

Electrodes of Co_3O_4@MnO_2@NiO/GO were marvelously invented using the hydrothermal technique for applications in supercapacitors. GO was integrated into the nanostructured electrodes synthesized due to its prominent surface area and electrical conductivity. The synergistic cooperation among these transition metals and GO improved electrode properties, life span, and stability). The estimated specific capacitance values from the GCD plots were 503, 697, 811, 242, and 215 Fg^{-1} for the pristine and electrodes irradiated with 2.5×10^{15}, 5.0×10^{15}, 7.5×10^{15}, and 1.0×10^{16} ions/cm^2

dosages respectively. Electrodes radiated with a carbon ion dosage of 5.0×10^{15} ions/cm^2 delivered the best specific capacitance, energy density, and power density, indicating that moderate carbon ion radiation improves the electrochemical properties of nanostructured Co_3O_4@MnO_2@NiO/GO electrode.

References

1. Obodo, R.M.; Shinde, N.M.; Chime, U.K.; Ezugwu, S.; Nwanya, A.C.; Ahmad, I.; Maaza, M.; Ezema, F.I. Recent advances in metal oxide/hydroxide on three-dimensional nickel foam substrate for high performance pseudocapacitive electrodes. *Curr. Opin. Electrochem.* **2020**, *21*, 242–249. [CrossRef]
2. Obodo, R.M.; Nwanya, A.C.; AEkwealor, B.C.; Ahmad, I.; Zhao, T.; Maaza, M.; Ezema, F. Influence of pH and annealing on the optical and electrochemical properties of cobalt (III) oxide (Co_3O_4) thin films. *Surf. Interfaces* **2019**, *16*, 114–119. [CrossRef]
3. Simon, P.; Gogotsi, Y.; Dunn, B. Where do batteries end and supercapacitors begin? *Science* **2014**, *343*, 1210–1211. [CrossRef] [PubMed]
4. Huang, Y.; Tang, Z.; Liu, Z.; Wei, J.; Hu, H.; Zhi, C. Toward enhancing wearability and fashion of wearable supercapacitor with modified polyurethane artificial leather electrolyte. *Nano-Micro Lett.* **2018**, *10*, 1–8. [CrossRef]
5. Nwachukwu, I.; Nwanya, A.; Osuji, R.; Ezema, F. Nanostructured Mn-doped CeO_2 thin films with enhanced electrochemical properties for pseudocapacitive applications. *J. Alloys Compounds* **2021**, *886*, 161206. [CrossRef]
6. Wu, Y.; Yang, Y.; Zhao, X.; Tan, Y.; Liu, Y.; Wang, Z.; Ran, F. A novel hierarchical porous 3D structured vanadium nitride/carbon membranes for high-performance supercapacitor negative electrodes. *Nano-Micro Lett.* **2018**, *10*, 1–11. [CrossRef]
7. Jabeen, N.; Hussain, A.; Xia, Q.; Sun, S.; Zhu, J.; Xia, H. High performance 2.6 V aqueous asymmetric supercapacitors based on in situ formed Na0.5MnO2 nanosheet assembled nanowall arrays. *Adv. Mater.* **2017**, *29*, 1700804. [CrossRef]
8. Bo, Z.; Li, C.; Yang, H.; Ostrikov, K.; Yan, J.; Cen, K. Design of Supercapacitor Electrodes Using Molecular Dynamics Simulations. *Nano-Micro Lett.* **2018**, *10*, 1–23. [CrossRef]
9. Obodo, R.M.; Nwanya, A.C.; Iroegbu, C.; Ezekoye, B.A.; Ekwealor, A.B.C.; Ahmad, I.; Ezema, F.I. Effects of swift copper (Cu^{2+}) ion irradiation on structural, optical and electrochemical properties of Co_3O_4-CuO-MnO_2/GO nanocomposites powder. *Adv. Powder Technol.* **2020**, *31*, 1728–1735. [CrossRef]
10. Zhang, J.; Chen, M.; Ge, Y.; Liu, Q. Manganese Oxide on Carbon Fabric for Flexible Supercapacitors. *J. Nanomater.* **2016**, *2016*, 1–8. [CrossRef]
11. Lv, H.; Pan, Q.; Song, Y.; Liu, X.X.; Liu, T. A Review on Nano-/Microstructured Materials Constructed by Electrochemical Technologies for Supercapacitors. *Nano-Micro Lett.* **2020**, *12*, 1–56. [CrossRef] [PubMed]
12. Liu, Y.; Soucaze-Guillous, B.; Taberna, P.L.; Simon, P. Understanding of carbon-based supercapacitors ageing mechanisms by electrochemical and analytical methods. *J. Power Sources* **2017**, *366*, 123–130. [CrossRef]
13. Jian, X.; Liu, S.; Gao, Y.; Tian, W.; Jiang, Z.; Xiao, X.; Tang, H.; Yin, L. Carbon-based electrode materials for supercapacitor: Progress, challenges and prospective solutions. *J. Electr. Eng.* **2016**, *4*, 75–87. [CrossRef]
14. Ratajczak, P.; Suss, M.E.; Kaasik, F.; Béguin, F. Carbon electrodes for capacitive technologies. *Energy Storage Mater.* **2019**, *16*, 126–145. [CrossRef]
15. Jiang, Y.; Liu, J. Definitions of pseudocapacitive materials: A brief review. *Energy Environ. Mater.* **2019**, *2*, 30–37. [CrossRef]
16. Brousse, T.; Bélanger, D.; Long, J.W. To be or not to be pseudocapacitive? *J. Electrochem. Soc.* **2015**, *162*, A5185–A5189. [CrossRef]
17. Augustyn, V.; Simon, P.; Dunn, B. Pseudocapacitive oxide materials for high-rate electrochemical energy storage. *Energy Environ. Sci.* **2014**, *7*, 1597–1614. [CrossRef]

18. Nwanya, A.C.; Obi, D.; Ozoemena, K.I.; Osuji, R.U.; Awada, C.; Ruediger, A.; Maaza, M.; Rosei, F.; Ezema, F.I. Facile Synthesis of Nanosheet-like CuO Film and its Potential Application as a High-Performance Pseudocapacitor Electrode. *Electrochim. Acta* **2016**, *198*, 220–230. [CrossRef]

19. Veerakumar, P.; Sangili, A.; Manavalan, S.; Thanasekaran, P.; Lin, K.C. Research Progress on Porous Carbon Supported Metal/Metal Oxide Nanomaterials for Supercapacitor Electrode Applications. *Ind. Res. E.C.* **2020**, *59*, 6347–6374. [CrossRef]

20. Lyu, L.; Seong, K.D.; Kim, J.M.; Zhang, W.; Jin, X.; Kim, D.K.; Jeon, Y.; Kang, J.; Piao, Y. CNT/High Mass Loading MnO_2/Graphene-Grafted Carbon Cloth Electrodes for High-Energy Asymmetric Supercapacitors. *Nano-Micro Lett.* **2019**, *11*, 88. [CrossRef]

21. Parveen, N.; Hilal, M.; Han, J.I. Newly Design Porous/Sponge Red Phosphorus@ Graphene and Highly Conductive Ni 2 P Electrode for Asymmetric Solid State Supercapacitive Device With Excellent Performance. *Nano-Micro Lett.* **2020**, *12*, 1–16. [CrossRef] [PubMed]

22. Zhang, Y.; Zhang, Y.; Zhang, Y.; Si, H.; Sun, L. Bimetallic $NiCo_2S_4$ Nanoneedles Anchored on Mesocarbon Microbeads as Advanced Electrodes for Asymmetric Supercapacitors. *Nano-Micro Lett.* **2019**, *11*, 35. [CrossRef] [PubMed]

23. Nwanya, A.C.; Jafta, C.J.; Ejikeme, P.M.; Ugwuoke, P.E.; Reddy, M.V.; Osuji, R.U.; Ozoemena, K.I.; Ezema, F.I. Electrochromic and electrochemical capacitive properties of tungsten oxide and its polyaniline nanocomposite films obtained by chemical bath deposition method. *Electrochim. Acta* **2014**, *128*, 218–225. [CrossRef]

24. Qi, Z.; Younis, A.; Chu, D.e.a. A Facile and Template-Free One-Pot Synthesis of Mn_3O_4 Nanostructures as Electrochemical Supercapacitors. *Nano-Micro Lett.* **2016**, *8*, 165–173. [CrossRef] [PubMed]

25. Li, Z.; Zhang, W.; Liu, Y.; Guo, J.; Yang, B. 2D nickel oxide nanosheets with highly porous structure for high performance capacitive energy storage. *J. Phys. D Appl. Phys.* **2018**, *51*, 045302. [CrossRef]

26. Ramesh, S.; Karuppasamy, K.; Yadav, H.e.a. Ni(OH)2-decorated nitrogen doped MWCNT nanosheets as an efficient electrode for high performance supercapacitors. *Sci. Rep.* **2019**, *9*, 6034. [CrossRef]

27. Yang, S.; Liu, Y.; Hao, Y.; Yang, X.; Goddard, W.A., III; Zhang, X.L.; Cao, B. Oxygen-vacancy abundant ultrafine Co_3O_4/graphene composites for high-rate supercapacitor electrodes. *Adv. Sci.* **2018**, *5*, 1700659. [CrossRef]

28. Nwanya, A.C.; Obi, D.; Osuji, R.U.; Bucher, R.; Maaza, M.; Ezema, F.I. Simple chemical route for nanorod-like cobalt oxide films for electrochemical energy storage applications. *J. Solid State Electrochem.* **2017**, *21*, 2567–2576. [CrossRef]

29. Bai, Y.; Liu, M.; Sun, J.; Gao, L. Fabrication of Ni-Co binary oxide/reduced graphene oxide composite with high capacitance and cyclicity as efficient electrode for supercapacitors. *Ionics* **2016**, *22*, 535–544. [CrossRef]

30. Uke, S.J.; Akhare, V.P.; Bambole, D.R.; Bodade, A.B.; Chaudhari, G.N. Recent advancements in the cobalt oxides, manganese oxides, and their composite as an electrode material for supercapacitor: A review. *Front. Mater.* **2017**, *4*, 21. [CrossRef]

31. Xu, J.; Xu, C.; Zhao, Y.; Wu, J.; Hu, J. Hollow Co_3O_4@MnO_2 Cubic Derived From ZIF-67@Mn-ZIF as Electrode Materials for Supercapacitors. *Front. Chem.* **2019**, *7*, 1–6. [CrossRef] [PubMed]

32. Singh, A.K.; Sarkar, D.; Karmakar, K.; Mandal, K.; Khan, G.G. High-performance supercapacitor electrode based on cobalt oxide–manganese dioxide–nickel oxide ternary 1D hybrid nanotubes. *ACS Appl. Mater. Interfaces* **2016**, *8*, 20786–20792. [CrossRef] [PubMed]

33. Arunpandiyan, S.; Selvameenakshi, C.; Ezhil Arasi, S.; Devendran, P.; Arivarasan, A. Effect of Redox Additive Electrolyte on the Electrochemical Performance of MnO_2 Nanorods for Supercapacitor Application. *Int. J. Innov. Technol. Explor. Eng. (IJITEE)* **2019**, *9*, 2278–3075.

34. Ghalmi, Y.; Habelhames, F.; Sayah, A.; Bahloul, A.; Nessark, B.; Shalabi, M.; Nunzi, J.M. Capacitance performance of NiO thin films synthesized by direct and pulse potentiostatic methods. *Ionics* **2019**, *25*, 6025–6033. [CrossRef]

35. Niveditha, C.V.; Aswini, R.; Fatima, M.J.; Ramanarayan, R.; Pullanjiyot, N.; Swaminathan, S. Feather like highly active Co_3O_4 electrode for supercapacitor application: A potentiodynamic approach. *Mater. Res. Express* **2018**, *5*, 065501. [CrossRef]

36. Ramesh, S.; Karuppasamy, K.; Kim, H.S.; Kim, J.H. Hierarchical Flowerlike 3D nanostructure of Co_3O_4@MnO_2/N-doped Graphene oxide (NGO) hybrid composite for a high-performance supercapacitor. *Sci. Rep.* **2018**, *8*, 1–11. [CrossRef]

37. Liu, Y.; Gao, C.; Li, Q.; Pang, H. Nickel oxide/graphene composites: Synthesis and applications. *Chem.–A Eur. J.* **2019**, *25*, 2141–2160. [CrossRef]

38. Ke, Q.; Wang, J. Graphene-based Materials for Supercapacitor Electrodes—A Review. *J. Mater.* **2016**, *2*, 37–54. [CrossRef]

39. Ramesh, S.; Karuppasamy, K.; Msolli, S.; Kim, H.S.; Kim, H.S.; Kim, J.H. A nanocrystalline structured NiO/MnO_2@ nitrogen-doped graphene oxide hybrid nanocomposite for high performance supercapacitors. *New J. Chem.* **2017**, *41*, 15517–15527. [CrossRef]

40. Chen, J.; Huang, Y.; Li, C.; Chen, X.; Zhang, X. Synthesis of NiO@MnO_2 core/shell nanocomposites for supercapacitor application. *Appl. Surf. Sci.* **2016**, *360*, 534–539. [CrossRef]

41. Mary, A.; Sathish, C.; Vinu, A.; Bose, A. Electrochemical performance of rGO/$NiCo_2O_4$@$ZnCo_2O_4$ ternary composite material and the fabrication of all-solid-state supercapacitor device. *Energy Fuels* **2020**, *34*, 10131–10141. [CrossRef]

42. Mary, A.; Sathish, C.; Kumar, P.; Vinu, A.; Bose, A. Fabrication of hybrid supercapacitor device based on $NiCo_2O_4$@$ZnCo_2O_4$ and the biomass-derived N-doped activated carbon with a honeycomb structure. *Electrochim. Acta* **2020**, *342*, 136062. [CrossRef]

43. Jung, M.; Park, M.; Lee, Y. Effects of E-Beam Irradiation on the Chemical, Physical, and Electrochemical Properties of Activated Carbons for Electric Double-Layer Capacitors. *J. Nanomater.* **2015**, *2015*, 240264. [CrossRef]

44. Obodo, R.M.; Ahmad, A.; Jain, G.H.; Ahmad, I.; Maaza, M.; Ezema, F.I. 8.0 MeV copper ion (Cu++) irradiation-induced effects on structural, electrical, optical and electrochemical properties of Co$_3$O$_4$-NiO-ZnO/GO nanowires. *Mater. Sci. Energy Technol.* **2020**, *3*, 193–200. [CrossRef]

45. Obodo, R.M.; Nwanya, A.C.; Iroegbu, C.; Ahmad, I.; Ekwealor, A.B.C.; Osuji, R.U.; Maaza, M.; Ezema, F.I. Transformation of GO to rGO due to 8.0 MeV carbon (C++) ions irradiation and characteristics performance on MnO$_2$–NiO–ZnO@GO electrode. *Int. J. Energy Res.* **2020**, *44*, 6792–6803. [CrossRef]

46. Ugarte, D. Curling and closure of graphitic networks under electron-beam irradiation. *Nature* **1992**, *395*, 707–709. [CrossRef]

47. Gómez-Navarro, C.; de Pablo, P.; Gómez-Herrero, J.; Biel, B.; Garcia-Vidal, F.; Rubio, A.; Flores, F. Tuning the conductance of single-walled carbon nanotubes by ion irradiation in the Anderson localization regime. *Nat. Mater.* **2005**, *4*, 534–539. [CrossRef]

48. Siraj, K.; Khaleeq-ur-Rahman, M.; Rafique, M.S.; Nawaz, T. Effect of 4MeV electron beam irradiation on carbon films. *Nucl. Instrum. Methods Phys. Res. Sect. B Beam Interact. Mater. Atoms* **2011**, *269*, 53–56. [CrossRef]

49. Li, X.; Liu, L.; Wang, X.; Ok, Y.; Elliott, J.; Chang, S.; Chung, H.-J. Flexible and Self-Healing Aqueous Supercapacitors for Low Temperature Applications: Polyampholyte Gel Electrolytes with Biochar Electrodes. *Sci. Rep.* **2017**, *7*, 1685. [CrossRef]

50. Momodu, D.; Bello, A.; Oyedotun, K.; Ochai-Ejeh, F.; Dangbegnon, J.; Madito, M.; Manyala, N. Enhanced electrochemical response of activated carbon nanostructures from tree-bark biomass waste in polymer-gel active electrolytes. *RSC Adv.* **2017**, *7*, 37286–37295. [CrossRef]

51. Wei, B.; D'Arcy-Gall, J.; Ajayan, P.; Ramanath, G. Tailoring structure and electrical properties of carbon nanotubes using kilo-electron-volt ions. *Appl. Phys. Lett.* **2003**, *83*, 3581. [CrossRef]

52. Krasheninnikov, A.; Banhart, F.; Li, J.; Foster, A.; Nieminen, R. Stability of carbon nanotubes under electron irradiation: Role of tube diameter and chirality. *Phys. Rev. B* **2005**, *72*, 125428. [CrossRef]

53. Banhart, F. Formation and transformation of carbon nanoparticles under electron irradiation. *Philos. Trans. A Math. Phys. Eng. Sci.* **2004**, *362*, 2205–2222. [CrossRef] [PubMed]

54. Farooq, A.; Aisida, S.; Jalild, A.; Dee, C.-F.; Ooi, P.; Sorokin, M.; Jabeen, N.; Ahmad, I.; Zhao, T.-K. C ions irradiation induced defects analysis and effects on optical properties of TiO$_2$ Nanoparticles. *J. Alloys Compd.* **2021**, *863*, 158635. [CrossRef]

55. Mao, S.; Wen, Z.H.; Kim, H.; Lu, G.H.; Hurley, P.; Chen, J.H. Nanohybrids for Energy Applications. *ACS Nano* **2012**, *6*, 7505–7513. [CrossRef]

56. Chaudhary, Y.; Khan, S.A.; Shrivastava, R.; Satsangi, V.R.; Prakash, S.; Avasthi, D.K.; Dass, S. A study on 170 MeV Au+13 irradiation induced modifications in structural and photo electrochemical behaviour of nanostructured CuO thin films. *Nucl. Instrum. Methods Phys. Res. Sect. B* **2004**, *225*, 291–296. [CrossRef]

57. Satoh, Y.; Yoshiie, T.; Ishida, I.; Kiritani, M. Defect structure development in electron-irradiated Cu-based Si, Ge, and Sn binary alloys. *Philos. Mag. A* **2000**, *80*, 2567–2590. [CrossRef]

58. Saravanakkumar, D.; Sivaranjani, S.; Kaviyarasu, K.; Ayeshamariam, A.; Ravikumar, B.; Pandiarajan, S.; Veeralakshmi, C.; Jayachandran, M.; Maaza, M. Synthesis and characterization of ZnO-CuO nanocomposites powder by modified perfume spray pyrolysis method and its antimicrobial investigation. *J. Semicond.* **2018**, *39*, 033001. [CrossRef]

59. Numan, A.; Duraisamy, N.; Omar, F.S.; Mahipal, Y.K.; Ramesha, K.; Ramesh, S. Enhanced electrochemical performance of cobalt oxide nanocube intercalated reduced graphene oxide for supercapacitor application. *RSC Adv.* **2016**, *6*, 34894–34902. [CrossRef]

60. Liu, H.; Gou, X.; Wang, Y.; Du, X.; Quan, C.; Qi, T. Cauliflower-like Co$_3$O$_4$/three-dimensional graphene composite for high performance supercapacitor applications. *J. Nanomater.* **2015**, *11*, 874245. [CrossRef]

61. Zhang, D.; Zou, W. Decorating reduced graphene oxide with Co$_3$O$_4$ hollow spheres and their application in supercapacitor materials. *Curr. Appl. Phys.* **2013**, *13*, 1796–1800. [CrossRef]

62. Aitahsaine, H.; Atourki, L.; Ezahri, M.; Bouabid, K.; Ihlal, A.; Villain, S.; Benlhachemi, A. Novel synthesis, characterization and optical properties of Lu2O3 deposited by electrochemical method. *Mater. Lett.* **2015**, *160*, 415–418. [CrossRef]

63. Ahmad, R.; Tripathy, N.; Ahn, M.-S.; Bhat, K.; Mahmoudi, T.; Wang, Y.; Yoo, J.-Y.; Kwon, D.-W.; Yang, H.-Y.; Hahn, Y.-B. Highly Efficient Non-Enzymatic Glucose Sensor Based on CuO Modified Vertically-Grown ZnO Nanorods on Electrode. *Sci. Rep.* **2017**, *7*, 5715. [CrossRef] [PubMed]

64. He, G.; Li, J.; Chen, H.; Shi, J. Hydrothermal preparation of Co$_3$O$_4$@ graphene nanocomposite for supercapacitor with enhanced capacitive performance. *Mater. Lett.* **2012**, *82*, 61–63. [CrossRef]

65. Park, S.K.; Suh, D.H.; Park, H.S. Electrochemical assembly of reduced graphene oxide/manganese dioxide nanocomposites into hierarchical sea urchin-like structures for supercapacitive electrodes. *J. Alloys Compd.* **2016**, *688*, 146–151. [CrossRef]

66. Li, Z.; An, Y.; Hu, Z.; An, N.; Zhang, Y.; Guo, B.; Zhang, Z.; Yanga, Y.; Wu, H. Preparation of a two-dimensional flexible MnO$_2$/graphene thin film and its application in a supercapacitor. *J. Mater. Chem. A* **2016**, *4*, 10618–10626. [CrossRef]

67. Nwanya, A.C.; Offiah, S.U.; Amaechi, I.C.; Agbo, S.; Ezugwu, S.C.S.T.; Osuji, R.U.; Maaza, M.; Ezema, F.I. Electrochromic and electrochemical supercapacitive properties of Room Temperature PVP capped Ni(OH)2/NiO Thin Films. Electrode for supercapacitive applications. *J. Mater. Sci. Mater. Electron.* **2015**, *26*, 2236–2242.

68. Nwanya, A.C.; Ndipingwi, M.M.; Ikpo, C.O.; Obodo, R.M.; Nwanya, S.C.; Botha, S.; Ezema, F.I.; Iwuoha, E.I.; Maaza, M. Zea mays lea silk extract mediated synthesis of nickel oxide nanoparticles as positive electrode material for asymmetric supercabattery. *J. Alloys Comp.* **2020**, *822*, 153581.

69. Iwueke, D.C.; Amechi, C.I.; Nwanya, A.C.A.; Ekwealor, A.B.C.; Asogwa, P.U.; Osuji, R.U.; Maaza, M.; Ezema, F.I. A novel chemical preparation of Ni(OH)2/CuO nanocomposite thin films for supercapacitive applications. *J. Mater. Sci. Mater. Electron.* **2015**, *26*, 2236–2242. [CrossRef]

70. González, A.; Goikolea, E.; Barrena, J.A.; Mysyk, R. Review on supercapacitors: Technologies and materials. *Renew. Sustain. Energy Rev.* **2016**, *58*, 1189–1206. [CrossRef]

71. Pawar, S.A.; Patil, S.D.; Shin, J.C. Transition of hexagonal to square sheets of Co_3O_4 in a triple heterostructure of $Co_3O_4/MnO_2/GO$ for high performance supercapacitor electrode. *Curr. Appl. Phys.* **2019**, *19*, 794–803. [CrossRef]

72. Li, X.; Miao, R.; Tao, B.; Miao, F.; Zang, F.; Chu, P.K. $Co_3O_4/MnO_2/Co(OH)2$ on nickel foam composites electrode with excellent electrochemical performance for supercapacitor. *Solid State Sci.* **2019**, *95*, 105941. [CrossRef]

73. Li, W.; Bu, Y.; Jin, H.; Wang, J.Z.J.; Wang, S.; Wang, J. The Preparation of Hierarchical Flowerlike NiO/Reduced Graphene Oxide Composites for High Performance Supercapacitor Applications. *Energy Fuels* **2013**, *27*, 6304–6310. [CrossRef]

74. Masood, A.; Shoukat, Z.; Rehman, A.R.; Shahid, Z.; Chadury, A.; Mahmood, A.; Ramay, S.; Razaq, A. Nickel hydroxide and lignocelluloses fibers based flexible paper electrodes for energy storage applications. *J. Mater. Sci. Mater. Electron.* **2019**, *30*, 14772–14780. [CrossRef]

75. Jiang, H.; Li, C.; Sun, T.; Ma, J. High-performance supercapacitor material based on Ni(OH)(2) nanowire-MnO_2 nanoflakes core–shell nanostructures. *Chem. Commun.* **2012**, *48*, 2606–2608. [CrossRef] [PubMed]

76. Majid, S.R. High performance super-capacitive behaviour of deposited manganese oxide/nickel oxide binary electrode system. *Electrochim. Acta* **2014**, *138*, 1–8.

77. Wan, H.; Jiang, J.; Ruan, Y.; Yu, J.; Zhang, L.; Chen, H.; Miao, L.; Bie, S. Direct Formation of Hedgehog-Like Hollow Ni-Mn Oxides and Sulfides for Supercapacitor Electrodes. *Part. Syst. Charact.* **2014**, *31*, 857–862. [CrossRef]

78. Sun, J.; Li, W.; Zhang, B.; Li, G.; Jiang, L.; Chen, Z.; Zou, R.; Hu, J. 3D core/shell hierarchies of MnOOH ultrathin nanosheets grown on NiO nanosheet arrays for high-performance supercapacitors. *Nano Energy* **2014**, *4*, 56–64. [CrossRef]

79. Xia, H.; Zhu, D.; Luo, Z.; Yu, Y.; Shi, X.; Yuan, G.; Xie, J. Hierarchically Structured $Co_3O_4@Pt@MnO_2$ Nanowire Arrays for High-Performance Supercapacitors. *Sci. Rep.* **2013**, *3*, 2978. [CrossRef]

80. Wang, H.; Ren, Q.; Brett, D.; He, G.; Wang, R.; Key, J.; Ji, S. Double-shelled tremella-like $NiO@Co_3O_4@MnO_2$ as a high performance cathode material for alkaline supercapacitors. *J. Power Sources* **2017**, *343*, 76–82. [CrossRef]

81. Wang, Z.; Pan, S.; Wang, B.; Qi, J.; Tang, L.; Liu, L. Asymmetric Supercapacitors Based on $Co_3O_4@MnO_2@PPy$ Porous Pattern Core-Shell Structure Cathode Materials. *J. Electrochem. Sci. Technol.* **2021**, *12*, 46–357. [CrossRef]

82. Singh, A.; Sarkar, D.; Khan, G.; Mandal, K. Designing one dimensional Co-Ni/Co_3O_4-NiO core/shell nano-heterostructure electrodes for high-performance pseudocapacitor. *Appl. Phys. Lett.* **2014**, *104*, 133904. [CrossRef]

83. Fink, M.; Eckhardt, J.; Khadke, P.; Gerdes, T.; Roth, C. Bifunctional α-MnO_2 and Co_3O_4 catalyst for oxygen electrocatalysis in alkaline solution. *ChemElectroChem* **2020**, *7*, 4822–4836. [CrossRef]

84. Xia, Q.; Hui, K.; Hui, K.; Kim, S.; Lim, J.; Choi, S.; Zhang, L.; Mane, R.; Yun, J.; Kim, H.K. Facile synthesis of manganese carbonate quantum dots/$Ni(HCO_3)_2$–$MnCO_3$ composites as advanced cathode materials for high energy density asymmetric supercapacitors. *J. Mater. Chem. A* **2015**, *3*, 22102–22117. [CrossRef]

85. Saykar, N.; Pilania, R.; Banerjee, L.; Mahapatra, S. Synthesis of NiO-Co_3O_4 Nano-sheets and its temperature dependent supercapacitive behaviour. *J. Phys. D Appl. Phys.* **2018**, *51*, 475501. [CrossRef]